Effects of Film Thickness on Electrochemical Properties of Nanoscale Polyethylenedioxythiophene (PEDOT) Thin-Films Grown by Oxidative Molecular Layer Deposition (oMLD)

Katrina G. Brathwaite, ^{1,†} Quinton K. Wyatt, ^{2,†} Amalie Atassi, ³ Shawn A. Gregory, ³ Eric Throm, ¹ David Stalla, ⁴ Shannon K. Yee, ⁵ Mark D. Losego, ³ Matthias J. Young ^{1,2,*}

¹Chemical and Biomedical Engineering, University of Missouri, Columbia, Missouri, 65211, United States

²Department of Chemistry, University of Missouri, Columbia, Missouri, 65211, United States

³School of Materials Science and Engineering, Georgia Institute of Technology, Atlanta, Georgia, 30332, United States

⁴Electron Microscopy Core Facility, University of Missouri, Columbia, Missouri, 65211, United States

⁵George W. Woodruff School of Mechanical Engineering, Georgia Institute of Technology, Atlanta, Georgia, 30332, United States

I. Abstract

Poly(3,4-ethylene dioxythiophene) (PEDOT) has a high theoretical charge storage capacity, making it of interest for electrochemical applications including energy storage and water desalination. Nanoscale thin films of PEDOT are particularly attractive for these applications to enable faster charging. Recent work has demonstrated that nanoscale thin films of PEDOT can be formed using sequential gas-phase exposures via oxidative molecular layer deposition, or oMLD, which provides advantages in conformality and uniformity on high aspect ratio substrates over other deposition techniques. But to date, the electrochemical properties of these oMLD PEDOT thin films have not been well-characterized. In this work, we examine the electrochemical properties of 5-100 nm thick PEDOT films formed using 20-175 oMLD deposition cycles. We find that film thickness of oMLD PEDOT films affects the orientation of ordered domains leading to a substantial change in charge storage capacity. Interestingly, we observe a minimum in charge storage capacity for an oMLD PEDOT film thickness of ~30 nm (60 oMLD cycles at 150°C), coinciding with the highest degree of face-on oriented PEDOT domains as measured using grazing incidence wide angle X-ray scattering (GIWAXS). Thinner and thicker oMLD PEDOT films exhibit higher fractions of oblique (off-angle) orientations and corresponding increases in charge capacity of up to 120 mAh/g. Electrochemical measurements suggest that higher charge capacity in films with mixed domain orientation arise from the facile transport of ions from the liquid electrolyte into the PEDOT layer. Greater exposure of the electrolyte to PEDOT domain edges is posited to facilitate faster ion transport in these mixed domain films. These insights will inform future design of PEDOT coated high-aspect ratio structures for electrochemical energy storage and water treatment.

[†]Authors contributed equivalently

^{*}email: matthias.young@missouri.edu

II. Introduction

Poly(3,4-ethylene dioxythiophene) (PEDOT) is a commonly used, easily processable, temperature-stable, electrically conductive polymer. Upon chemical or electrochemical oxidation, cation radicals form along the polymer backbone of PEDOT that act as charge carriers for electrical conductivity and are the source of reversible electrochemical charge capacity, as depicted in Figure 1a. The electrical conductivity of PEDOT often surpasses other conjugated polymers due to ethylene oxide groups on each 3,4-ethylene dioxythiophene (EDOT) monomer, which served to block reaction at the C_{β} positions of thiophene, and to act as electron donating groups to increase the susceptibility to oxidative doping. In recent years, PEDOT has been used for bioelectronic devices, optoelectronics, thermoelectrics, light emitting diodes (LEDs), chemical sensors, electrochemical energy storage, organic photovoltaics, desalination, nanoelectronics, and much more. Polymers

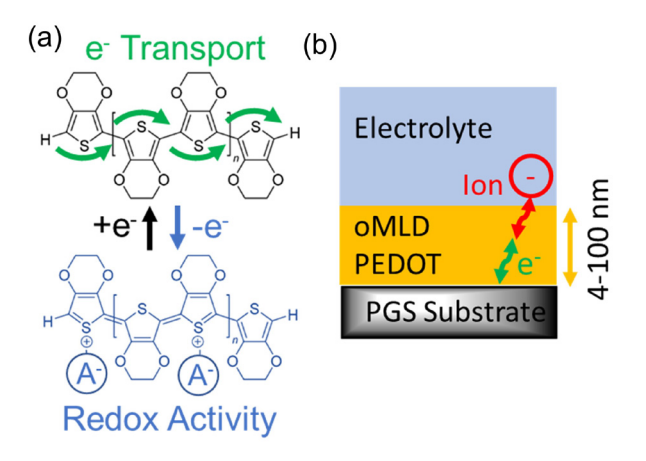


Figure 1. (a) Chemical structure of PEDOT showing the reduced (green) and oxidized (blue) forms. PEDOT is electrically conductive and redox active making it attractive for electrochemical applications including energy storage and water treatment. This work examines the electrochemical behavior of (b) nanoscale thin films of PEDOT formed by oxidative molecular layer deposition (oMLD).

In particular, PEDOT's electrical and electrochemical properties make it appealing in electrochemical devices: as a protective coating for Li-ion and other alkali-ion batteries, ^{14–16} as an active material for supercapacitor electrodes for high power energy storage, ^{13,17} and as an electrode material for electrochemical water desalination. ^{18,19} Thin films of PEDOT are more attractive for these applications. This is because thinner films reduce the length scale for solid-state ionic and electronic transport, theoretically reducing diffusion overpotentials when used as protective coatings, and yielding higher specific electrochemical charge storage capacity when used as an active material in energy storage and water desalination. The benefits of nanoscale film thicknesses to enhance charge capacity have been shown, for example, in prior work on nanoscale PANI, which measured specific charge capacities of >130 mAh/g at thicknesses of < 30 nm, ²⁰ and in prior work on nanoscale PPY, which exhibited capacities of >250 mAh/g for < 30 nm thicknesses. ^{21,22} However, conventional techniques for PEDOT synthesis such as (a) homogeneous oxidative

chemical polymerization using a chemical oxidant such as iron(III) chloride (FeCl₃),² or (b) electrochemical oxidation⁴ cannot easily deliver uniform nanoscale films of < 100 nm.

In the last thirty years, gas phase polymerization techniques have been developed to form PEDOT and other polymers as uniform films with nanoscale thickness control.^{23–25} Gas phase polymerization of PEDOT has been performed using vapor phase polymerization (VPP) starting in 2003, ²⁶ oxidative chemical vapor deposition (oCVD)²⁷ starting in 2006, and oxidative molecular layer deposition (oMLD)²⁸ starting in 2014. In VPP, a gas-phase monomer (EDOT) is delivered to a substrate coated with a non-volatile chemical oxidant, where it reacts to form polymer films. In oCVD, EDOT and a choice of oxidant (e.g. FeCl₃) are mixed simultaneously in the gas phase and react to form polymer chains. In oMLD, the monomer (EDOT) and a volatile chemical oxidant such as molybdenum pentachloride (MoCl₅) are dosed in alternating vapor-phase exposures with an inert carrier gas purge between each precursor pulse. Because oCVD and oMLD do not require the use of side-chains or additives common in solution processing, they allow for the formation of chemically pure PEDOT thin films, and have been used to produce record electrical conductivities for PEDOT in excess of 6000 S/cm.^{29,30} Of these vapor phase polymer deposition techniques, oMLD is particularly appealing for the electrochemical applications described above because oMLD proceeds via self-limiting reactions on material surfaces, providing improved uniformity and conformality on 3D substrates, 21,28 similar to other molecular layer deposition (MLD) processes.31-33

In this study, we examine the electrochemical properties of 5-100 nm thick films of PEDOT grown by oMLD as depicted in Figure 1b, all formed at a fixed deposition temperature of 150°C. A few previous studies have examined the electrochemical properties of PEDOT thin films grown by oCVD, ^{34–36} but to our knowledge no studies have been published on the electrochemical charge storage properties of oMLD PEDOT. Although oCVD and oMLD are similar process, PEDOT films grown using these two methods exhibit different microstructures and properties. For example, oCVD PEDOT films exhibit primarily edge-on PEDOT orientation at temperatures ≤200°C and film thicknesses > 100 nm,³⁷ while oMLD PEDOT films exhibit primarily face-on domain orientation even at a low deposition temperature of 150°C and high (≥100 nm) film thickness.²⁸ These differences in the orientation of ordered PEDOT domains correlate with differences in electronic conductivity. oCVD PEDOT requires a deposition temperature >200°C and a film thickness of < 50 nm to achieve electronic conductivities of > 1000 S/cm, ³⁷ while oMLD PEDOT achieves electrical conductivities of >1000 S/cm at 150°C and ≥100 nm film thicknesses.²⁸ While the differences between the orientation of ordered domains and the electronic properties of PEDOT grown using oCVD and oMLD have been examined in prior work, ^{28,30,38–40} it is unclear how these differences translate to the electrochemical redox activity of PEDOT. This is of particular importance for <100 nm film thicknesses, where the microstructure and electronic properties of PEDOT have been found to vary greatly depending on deposition technique and temperature. Here, we study the crystalline structure and resultant electrochemical properties of nanoscale thin films of PEDOT grown by oMLD to inform its deployment in electrochemical technologies.

Results and Discussion

The electrochemical charge capacity of a PEDOT film is expected to increase with increasing film thickness. Thus, to evaluate the specific charge capacity (charge per unit mass) of oMLD PEDOT films, we must first establish control over film thickness. To this end, we performed a sequence of depositions on Si at varying numbers of oMLD cycles and measured the PEDOT film thickness for each deposition using neutron reflectivity (NR). In prior work, we reported saturating dose conditions for sequential pulses of EDOT and MoCl₅ at 150°C using in situ quartz crystal microbalance (QCM) measurements.²² These saturating conditions consisted of an MoCl₅ dose time of 100 s, an EDOT dose time of 20 s, and 100 s purge times after each precursor dose. Here, we employ these growth conditions to deposit PEDOT thin films on Si and pyrolytic graphite sheet (PGS) samples using between 20 and 175 oMLD cycles. In Figure 2a, we report NR for PEDOT films deposited on Si wafers using between 20 and 100 oMLD cycles. Overall, as the number of oMLD cycles increases, we observe narrower Kiessig fringes in the NR data, indicating thicker PEDOT layers. Samples deposited using 100 or more oMLD cycles did not yield NR data with defined Kiessig fringes. The NR traces in Figure 2a for between 20 and 80 oMLD cycles were modeled using Reflpak, 41 which utilizes the Parrat Method, 42 and fitted traces are shown in red in Figure 2a. These model fits account for the substrate, native oxide, and PEDOT film layers. Thickness values from these model fits agree with estimates using the Kiessig fringe widths visible in Figure 2a. At 20 oMLD cycles, the NR scattering data is indistinguishable from a bare Si wafer, corresponding to a 0.0 nm PEDOT thickness. We observe clear Kiessig fringes for samples formed by 40, 60, and 80 oMLD cycles, corresponding to fitted model thicknesses of 3.9, 27.1, and 39.8 nm, respectively. At 100 oMLD cycles, the Kiessig fringes are not well-defined, and the NR data is noisy, indicating the formation of a multi-phase or rough surface after 80 oMLD cycles.

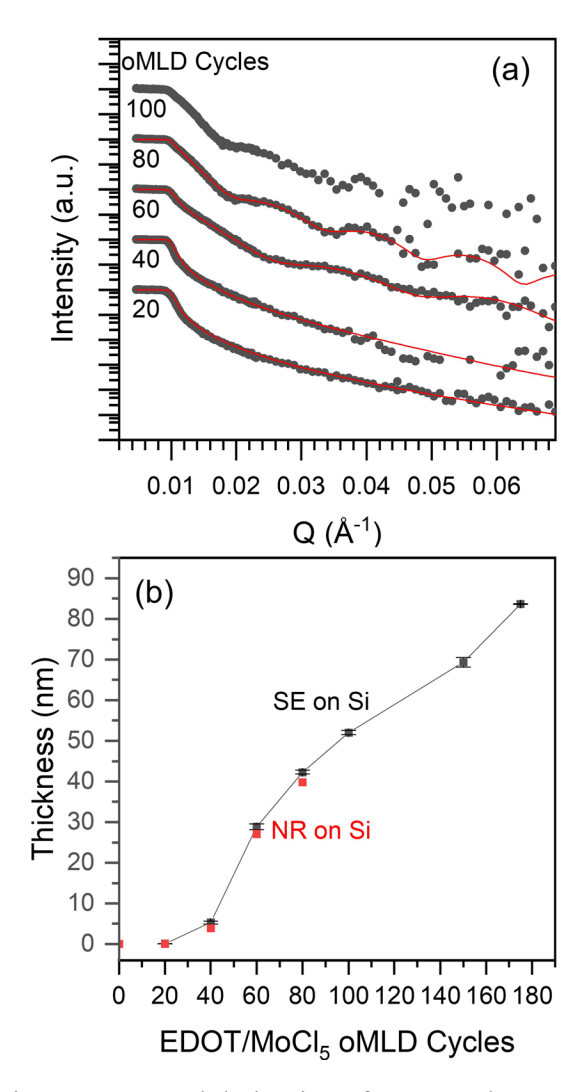


Figure 2. Growth behavior of PEDOT by EDOT/MoCl₅ oMLD including (a) NR data for PEDOT thin films on Si deposited using various numbers of oMLD cycles where the black circles are raw NR data and the red lines are model fits, and (b) comparison between NR fitted thicknesses and SE model thickness for PEDOT. ⁴²

Because the thickness of samples deposited using >80 oMLD cycles could not be determined by NR, we employed spectroscopic ellipsometry (SE) to determine the thickness of these thicker films of PEDOT. Here, we established the optical properties PEDOT films by performing SE measurements on the NR samples in Figure 2a. We note that the oMLD PEDOT films contain residual MoCl_x, oxidant and are in a fully oxidized state as-formed.^{22,28} These fully oxidized PEDOT films exhibit minimal optical absorption at wavelengths < 900 nm,^{4-7,43,44} allowing for facile SE thickness fitting using a simple Cauchy model for thicknesses from 0 - 60 nm. This SE fitting yielded a refractive index of 1.61 at a wavelength of 589 nm, consistent with a value of n = 1.6 reported previously.⁴⁵ The modeled SE thicknesses agreed with NR thicknesses within 3 nm. SE fits yielded thicknesses of 5.3, 28.9, 42.3, and 52.0 nm for 40, 60, 80, and 100 oMLD cycles, respectively. Interestingly, although this Cauchy model fit SE data for 40-100 oMLD cycles well,

this model did not capture the optical properties observed for 150 and 175 oMLD cycle samples by SE. We attribute this to a decrease in the state of oxidation of the as-deposited PEDOT films at higher film thicknesses. ^{46,47} To determine the thicknesses of these thicker films from the SE data, we employed an optical model comprising three Lorentz oscillators which captured the optical absorption observed in SE data for thicker films, yielding film thicknesses of 69.3 and 83.6 nm for 150 and 175 oMLD cycles, respectively. We observe a thickness of only ~5 nm after 40 oMLD cycles, which we attribute to a nucleation delay in formation of the PEDOT films on Si substrates. After 40 oMLD cycles we observe a steep increase in thickness vs. the number of oMLD cycles, and then a gradual levelling off to a steady-state growth rate of 0.45 nm/cycle between 60 and 175 oMLD cycles. We note that one EDOT monomer is ~0.4 nm in width and ~0.7 nm in length, such that a growth rate of 0.45 nm/cycle corresponds to the addition of ~1 monomer per growth cycle in a vertical growth direction. ^{48,49}

After establishing a growth curve of the PEDOT films on Si wafers, we then proceeded to measure the electrochemical properties of PEDOT films on PGS substrates which were included in the same reaction runs as the Si wafers studied in Figure 2. We examined the electrochemical charge storage capacity for these different film thicknesses using cyclic voltammetry (CV) in Figure 3. These CV data were collected in aqueous 0.1 M Na₂SO₄ at circumneutral pH under continuous argon purge at a sweep rate of 50 mV/s. We report CVs for PEDOT thin films formed using 20, 40, 60, 80, 100, and 150 oMLD cycles (panels a-f, respectively) on PGS substrates. We observe the emergence of typical CV character expected for PEDOT after 150 oMLD cycles, with two equilibrium potentials at -0.4 and 0.1 V vs. Ag/AgCl,4 corresponding to anion insertion redox processes and structural reconfiguration, respectively. 50,51 We calculate the charge storage on the oxidizing sweep, Q_{ox} , for each curve in Figure 3a-f as the area under the curve Q_{ox} = $\frac{1}{v}\int_{V_0}^{V_f} i(V) dV$ where V₀ is the lower limit of potential (here -0.75 V vs. Ag/AgCl), V_f is the upper limit of potential (here 0.75 V vs. Ag/AgCl), i(V) is the current measured at each potential, and v is the sweep rate, e.g. in mV/s and plot Q_{ox} vs. number of oMLD cycles in Figure 3g. In general, we would expect that increasing the number of oMLD cycles would lead to a thicker PEDOT layer and an increase in charge storage in Figure 3g, as has been observed for organic and inorganic redox-active thin films in previous work. 20,21,52-54. 450,51 However, surprisingly, as the number of oMLD cycles increases from 20 to 40 and from 40 to 60 oMLD cycles we observe sequentially lower charge capacities, where the 60 oMLD cycle condition provides the lowest amount of charge storage. This is not in line with previous results where thicker films yield higher charger capacities for

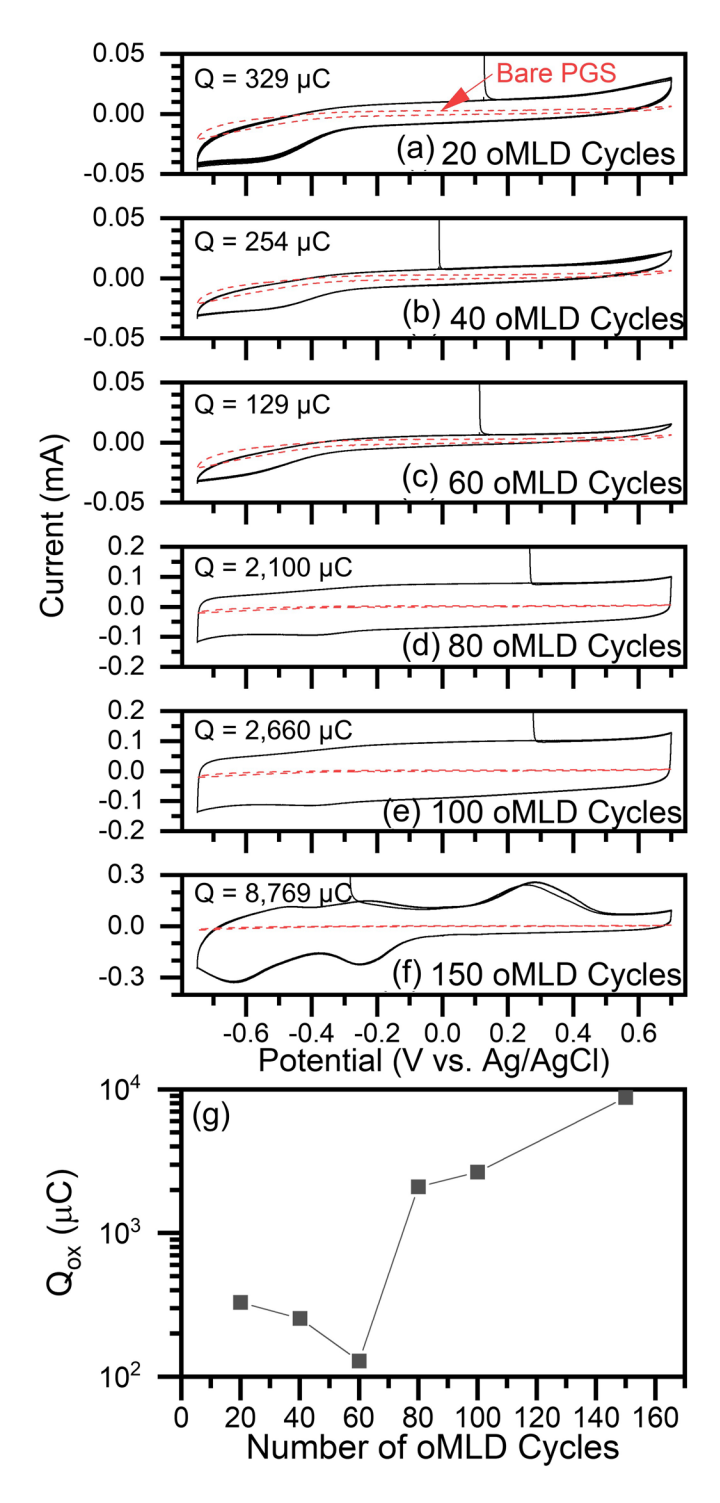


Figure 3. (a) CV electrochemical response curves of oMLD deposited PEDOT films (a 20, b 40, c 60, d 80, e 100, and f 150 oMLD cycles) on PGS (substrate) over a 1.5 V (-0.75 \rightarrow 0.75 V) potential window in 0.1 M Na₂SO₄ solution with 50 mV/s sweep rate showing (g) a minimum in the amount charge storage after 60 oMLD cycles.

This surprising observation of the lowest charge capacity after 60 oMLD growth cycles could arise from either (a) an anomaly in growth behavior on the PGS substrates where the amount of material

on PGS is not consistent with measurements on Si or (b) thickness-dependent differences in polymer microstructure which impact electrochemical properties. To begin to understand the origins of this effect, we set out to confirm the PEDOT thicknesses on PGS substrates. For this, we first employed scanning electron microscopy (SEM) to measure the thickness of PEDOT films deposited on PGS substrates grown using 60 and 100 oMLD cycles. We note that the <10 nm PEDOT film thicknesses expected for the 20 and 40 oMLD cycle conditions are too small to be readily observable by SEM. In Figure 4a and 4b, we measure mean PEDOT thicknesses of 33 \pm 3 nm and 66 ± 3 nm for films deposited using 60 and 100 oMLD cycles, respectively, each based on five SEM measurements on each sample, as depicted. These mean thickness values are approximately the same (only 4 and 11 nm higher, respectively) as the thicknesses of 28.9 and 52.0 nm measured on Si wafers after 60 and 100 oMLD cycles in Figure 2 and do not reflect an anomalously low thickness for the 60 oMLD cycle condition. We note Si wafers were included in the same deposition runs along with the PGS substrates and the thicknesses on these Si wafers were consistent with the thickness values presented in Figure 2. This data provides an indication that the lower electrochemical capacity we measure for the 60 oMLD cycle condition in Figure 3c does not arise from an anomalously lower amount of material on PGS at this number of oMLD cycles.

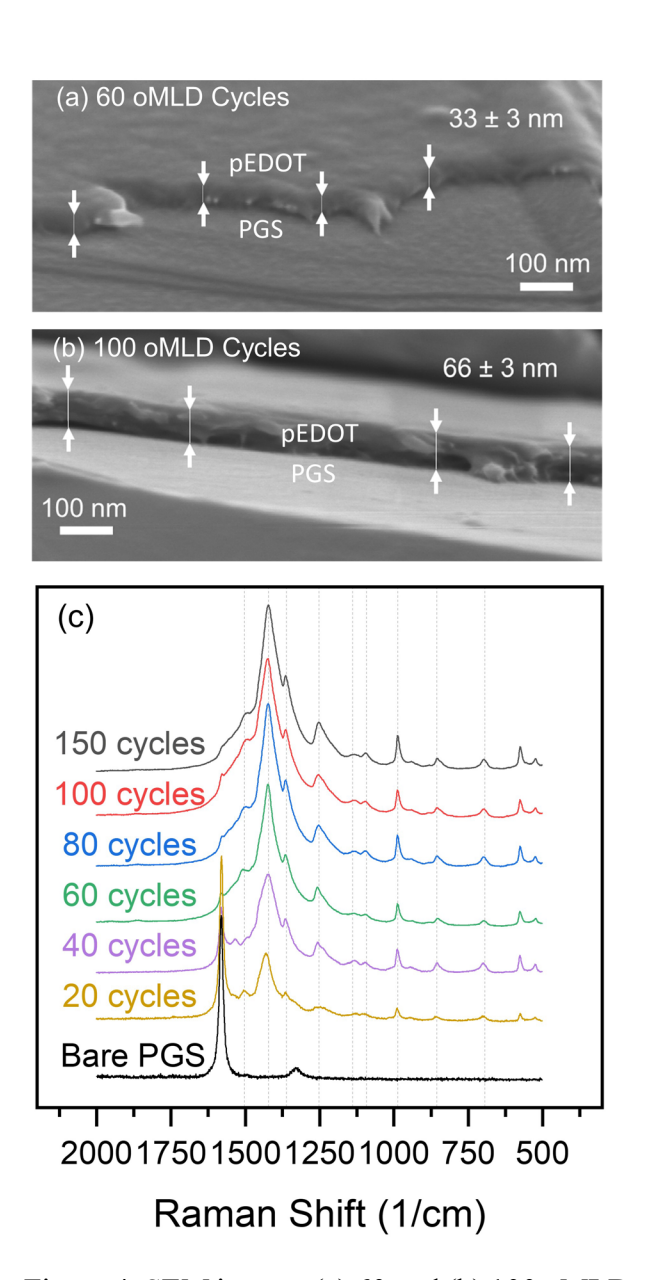


Figure 4. SEM images (a) 60 and (b) 100 oMLD cycles of PEDOT films on cleaved PGS substrates and (c) Raman spectra of PEDOT oMLD deposited films with reference lines for PEDOT.⁵⁵ The Raman spectra in (c) are scaled to emphasize the PEDOT Raman peaks in each sample.

Another possible explanation for the surprising trend in charge capacity vs. number of oMLD cycles we observe in Figure 3 could be the unexpected formation of thicker PEDOT films at the 20 and 40 oMLD cycle conditions on PGS substrate. To confirm a monotonic increase in thickness for the 20, 40, and 60 oMLD cycle samples we employed Raman spectroscopy measurements. In Figure 4c we report the Raman spectroscopy data for PEDOT-coated PGS sample formed using 20, 40, 60, 80, 100, and 150 oMLD cycles. The vertical dashed lines in Figure 4c are reference Raman lines for PEDOT. For all numbers of oMLD cycles, we observe the dominant Raman peaks for PEDOT at 1422, 1362, 1253, and 988 cm⁻¹, corresponding to symmetric C_{α} = C_{β} (-O) stretch, C_{β} - C_{β} stretch, C_{α} - C_{α} -(inter-ring) stretch, and ethoxylene ring deformation, respectively. 55

We also observe minor peaks at 1503, 1139, 1092, 856, and 694 cm⁻¹, corresponding to asymmetric C=C stretch, C-O-C deformation, and symmetric C-S-C deformation in PEDOT, respectively.⁵⁵ The Raman spectra for PEDOT films in Figure 4c are also consistent with previous oMLD and oCVD literature^{11,56–58} In general, as the number of oMLD cycles increases, we observe an increase in intensity of the characteristic PEDOT peaks in Figure 4c, indicating that the PEDOT film thickness increases monotonically with the number of oMLD growth cycles.

In addition to the increase in PEDOT Raman signal, we also observe a decrease in the Raman signal from the underlying PGS substrate with increasing number of oMLD cycles, indicating that the PEDOT film thickness is increasing and preventing Raman sampling from the substrate. Specifically, as the number of oMLD cycles increases, we observe a decrease in the peak at 1580 cm⁻¹ in Figure 4c, which corresponds to the graphitic G-band from the PGS substrate.^{59,60} For the thinnest films (<60 oMLD cycles) where this G-band peak is still prominent above the background PEDOT Raman signal, we calculate PEDOT film thicknesses based on the attenuated Raman signal of the underlying substrate. 61 Calibrating this analysis to the 33 nm PEDOT thickness after 60 oMLD cycles based on SEM analysis in Figure 4a, we calculate thicknesses of 4.0 nm and 9.2 nm for PEDOT films grown on PGS using 20 and 40 oMLD cycles, respectively. We note that although 20 oMLD cycles yielded a thickness of 0 nm on Si, we see a clear PEDOT Raman features after 20 oMLD cycles in Figure 4c, consistent with the deposition of a PEDOT film onto PGS after this number of oMLD cycles. We note that we measure ~4 nm higher thicknesses on PGS substrates relative to Si for the 20, 40 and 60 oMLD cycle conditions. We attribute this to differences in adsorption and growth characteristics of π -aromatic EDOT molecules onto graphitic carbon PGS surface compared with the native silicon oxide present on Si substrates. For reference, the adsorption of benzene onto SiO₂ has been measured to have an adsorption energy of -16 kJ/mol,⁶² whereas the adsorption of benzene onto graphene has an adsorption energy of -22 kJ/mol by DFT calculations. 63 This more favorable adsorption of π -aromatic molecules onto graphene would be expected to facilitate more rapid film nucleation of oMLD PEDOT onto graphitic substrates like PGS. As noted above in the discussion of Figure 2b, we observe a nucleation delay of >20 oMLD cycles on Si substrates, consistent with the weaker adsorption of EDOT onto native SiO₂ on Si wafers we describe here.

After establishing the thicknesses of oMLD PEDOT films on PGS substrates using SEM and Raman characterization, we reevaluate the electrochemical charge storage capacity of these films accounting for the total material mass. In Figure 5, we plot the specific charge storage capacities vs. cycle number from CV data collected up to 100 CV cycles at a sweep rate of 50 mV/s. Here we calculate the net charge arising from redox reactions in the PEDOT film as $Q_{net} = Q_{Ox}$ -Q_{PGS}, where Q_{PGS} is the capacity arising from double layer charge storage measured on a bare PGS substrate from a control experiment (Q_{PGS} = 22.63 nAh at a sweep rate of 50 mV/s). We then divide Q_{net} in each CV cycle by the total mass of PEDOT at each number of oMLD cycles. The mass of the PEDOT film, m, is calculated as $m = \rho V$, where $\rho = 1.5$ g/cm³ is taken as the density of PEDOT, ^{48,49} and the volume of the film is $V = t\pi r^2$, where t is the thickness of the film, and r = 0.635 cm is the radius of the circular area exposed to the electrolyte for these CV measurements. The thickness, t, of the 60 and 100 oMLD cycle films were taken to be 33 and 66 nm, respectively based on SEM imaging in Figure 4a and 4b. The thicknesses of the 20 and 40 oMLD cycle films

were taken to be 4.0 and 9.2 nm, respectively based on Raman analysis calibrated to the 60 oMLD cycle sample SEM thickness (described above in the discussion surrounding Figure 4c). The thickness of the 80 oMLD cycle sample was taken to be 50 nm – the average of the 60 and 100 oMLD cycle films measured by SEM in Figure 4a and 4b. Using these thickness values, we calculate specific mass capacities on the third CV cycle for 20, 40, 60, 80, and 100 PEDOT oMLD cycle films of 133, 71, 31, 112, and 101 mAh/g, respectively. After 100 CV cycles, we measure specific charge capacities of 71, 36, 12, 62, and 59 mAh/g at a sweep rate of 50 mV/s for 20, 40, 60, 80, and 100 oMLD cycles, respectively. With the exception of the samples grown using 40 and 60 oMLD cycles, these steady-state specific mass capacities of ~65 mAh/g after 100 CV cycles are consistent with values reported previously for bulk PEDOT. 13 We observe the highest specific charge capacity (133 mAh/g on the third CV cycle) for the thinnest (4 nm) PEDOT film grown using 20 oMLD cycles. This observation is consistent with previous reports showing that thinner films of redox active films (both organic and inorganic) yield higher electrochemical capacities arising from a shorter length scale for solid state ion diffusion. 20,21,52-54 We note that the specific capacities of 100-140 mAh/g we measure during initial CV cycling for 20, 80 and 100 oMLD cycle PEDOT films are a factor of ~2 higher than typical values. 13 These values are ~60% of the theoretical limit of 190 mAh/g for PEDOT, ¹³ and are similar to the highest capacities of ~120 mAh/g measured for nanoscale (200-300 nm) films of PEDOT grown by oCVD.³⁵

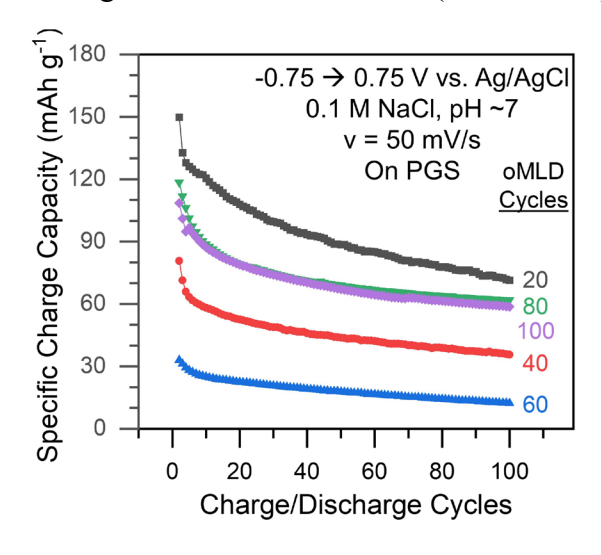


Figure 5. Specific electrochemical charge capacity of PEDOT films formed using 20, 40, 60, 80, and 100 oMLD cycles vs. the number of charge/discharge cycles up to 100 cycles, as measured using CV in aqueous 0.1 M NaCl at a sweep rate of 50 mV/s. ~30 nm PEDOT films formed using 60 oMLD cycles exhibit the lowest charge capacity of all film thicknesses.

Consistent with the lower charge capacity measured in Figure 3c, we also observe the lowest specific charge capacity for the 60 oMLD cycle condition in Figure 5. The specific capacity on the third CV cycle is only 31 mAh/g, and decreases after 100 CV cycles to 12 mAh/g. On average, over the 100 CV cycles shown in Figure 5, the 60 oMLD cycle condition (33 nm PEDOT thickness) exhibits a specific charge capacity that is $60 \pm 3\%$ lower than the 40 oMLD cycle (9 nm PEDOT thickness) condition, and $74 \pm 3\%$ lower than the 100 oMLD cycle (66 nm PEDOT thickness) condition. As shown in Figure 4c, the Raman features observed for the PEDOT film

deposited at 60 oMLD cycles are equivalent to the PEDOT formed using 40 or 100 oMLD cycles, and we therefore do not expect that the lower capacities arise from differences in chemical structure. We therefore hypothesized that the decrease in electrochemical capacity for the 60 oMLD cycle film originated from differences in microstructure within the PEDOT film at different film thicknesses formed using varying numbers of oMLD cycles. ²⁹³⁴

To examine this hypothesis, we performed grazing incidence wide-angle X-ray scattering (GIWAXS), to measure differences in ordered PEDOT domain orientation between 40, 60, and 100 oMLD cycle PEDOT films as depicted in Figure 6a, 6b, and 6c, respectively. Here, Si wafer substrates were employed to provide an optically flat surface for GIWAXS measurements. The raw 2D X-ray scattering data for 40, 60, and 100 oMLD PEDOT cycles are shown in the top row (panel i) of Figure 6. The dashed red semicircle in each panel (i) traces the constant value of q = 1.82 Å⁻¹, corresponding to the (020) lattice spacing for PEDOT. 30,35,64,65 The location around this semicircle of radius 1.82 Å⁻¹ is indicated by the azimuthal angle, χ where the vertical direction in the 2D scattering data corresponds to $\chi = 0^{\circ}$ and the horizontal direction corresponds to $\chi = 90^{\circ}$. The surface of each Si sample is aligned horizontally in the xy plane for these GIWAXS measurements, so scattering intensity observed in the vertical direction at $q_z = 1.82 \text{ Å}^{-1}$ ($\chi = 0^{\circ}$) indicates that the (020) PEDOT lattice plane is parallel with the sample surface, (i.e. PEDOT domains are in a face-on orientation as depicted in the insets the top row in Figure 6). Likewise, scattering intensity observed in the horizontal direction at $q_{xy} = 1.82 \text{ Å}^{-1} (\chi = 90^{\circ})$ indicates that the (020) PEDOT lattice plane is perpendicular to the sample surface, i.e. PEDOT domains are in an edge-on orientation. We observe differences in the relative scattering intensity as a function of azimuthal angle indicating that the PEDOT domains in each sample exhibit different distributions of PEDOT domain orientations.

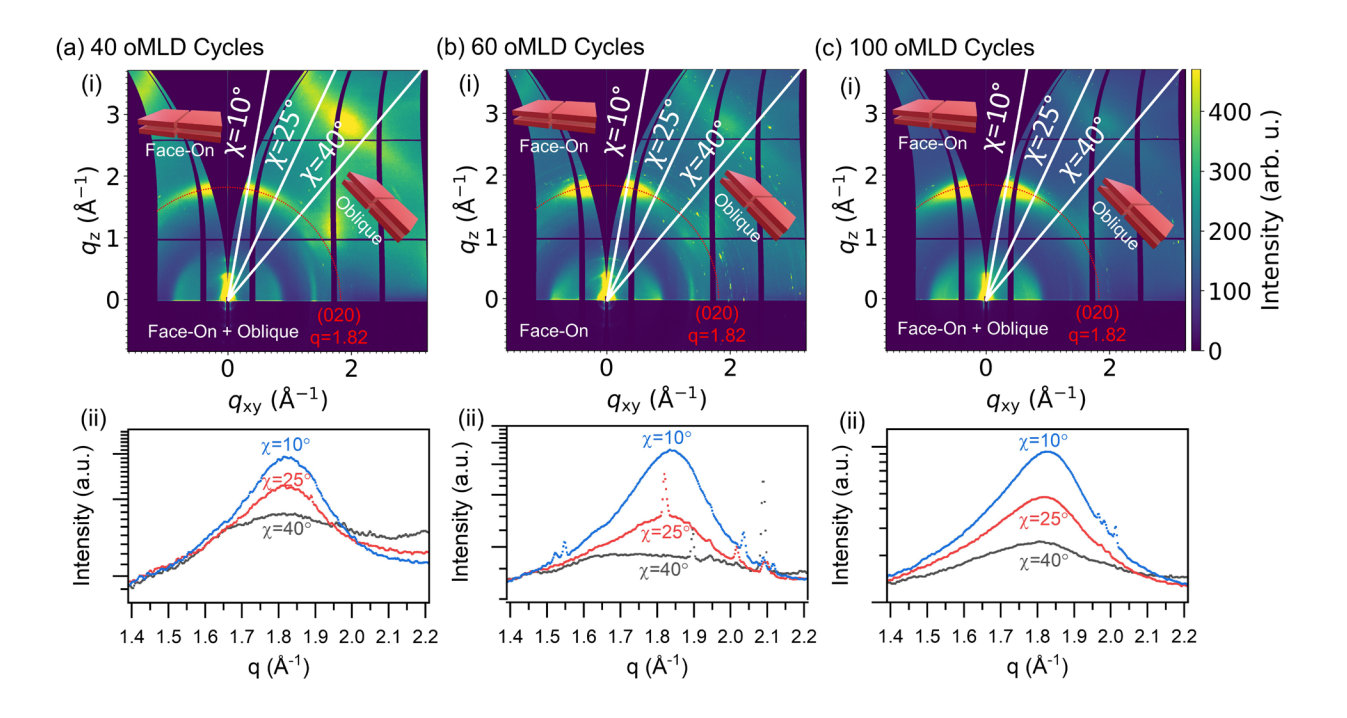


Figure 6. GIWAXS data for (a) 40, (b) 60, and (c) 100 oMLD cycles indicates that PEDOT domain orientation changes with the number of oMLD cycles. Raw 2D GIWAXS data (top row), showing primarily face-on orientation of PEDOT oMLD films of 40, 60, and 100 oMLD cycles, with some domains at oblique angles to the surface. Further GIWAXS data analysis (bottom row) of peak height at radial position of $q=1.82~\text{Å}^{-1}$ corresponding to the (020) PEDOT plane at azimuthal angles of $\chi=10^\circ$, $\chi=25^\circ$, and $\chi=40^\circ$ (indicated with white lines in the top row) shows a higher fraction of face-on oriented domains for 60 oMLD cycles compared with 40 and 100 oMLD cycles.

To analyze the relative amount of PEDOT domains oriented at different angles from surface parallel, we plot the scattering intensity as a function of q from 1.4 - 2.2 Å⁻¹ at constant values of $\chi = 10^{\circ}$, $\chi = 25^{\circ}$, and $\chi = 40^{\circ}$ for 40, 60 and 100 oMLD cycles in the bottom row (panel ii) of Figures 6a, 6b, and 6c, respectively. For each of these line scans, the raw 2D scattering data was integrated over a range of 5 azimuthal degrees centered on the indicated angle χ . For this analysis, the relative peak intensity at each value of χ is an indicator of the relative quantity of PEDOT oriented at an angle χ away from surface parallel. We note that data in the vertical direction at $\chi = 0^{\circ}$ is not available from GIWAXS scans due to the geometry of the projection of the Ewald sphere onto the 2D area detector. Evaluation 60,61 Likewise, the signal at $\chi > 40^{\circ}$ from PEDOT domains is obfuscated by scattering signal arising from the bare Si substrate, which is visible, for example, in Figure 6a.i as a spot centered at the coordinates $q_{xy} = 1.7$ Å⁻¹ and $q_z = 1.2$ Å⁻¹. For each of the 40, 60, and 100 oMLD cycle conditions in Figure 6a, 6b, and 6c, respectively, we observe the strongest scattering intensity at $\chi = 10^{\circ}$. This indicates that PEDOT domains are predominantly oriented face-on relative to the sample surface for all PEDOT thicknesses.

However, the amount of PEDOT domains oriented at oblique angles of $\chi = 25^{\circ}$ and $\chi = 40^{\circ}$ relative to $\chi = 10^{\circ}$ varies with the number of oMLD cycles. For the 40 oMLD cycle condition in Figure 6a.ii (5.3 nm PEDOT film thickness by SE) the scattering intensity at $\chi = 25^{\circ}$ and $\chi = 40^{\circ}$ are 72% and 40%, respectively, of the peak scattering intensity at $\chi = 10^{\circ}$. This indicates that for every unit quantity of PEDOT rotated at an angle of $\chi = 10 \pm 2.5^{\circ}$ away from surface parallel, 0.72 units of PEDOT are oriented at an angle $\chi = 25 \pm 2.5^{\circ}$ away from surface parallel, and 0.40 units of PEDOT domains are oriented at an angle $\chi = 40 \pm 2.5^{\circ}$ away from surface parallel. For the 60 oMLD cycle sample in Figure 6b.ii (28.9 nm PEDOT film thickness by SE), we observe a sharp drop-off in intensity for $\chi=25^{\circ}$, and no distinguishable peak at q=1.82 Å⁻¹ for $\chi=40^{\circ}$. The scattering intensities above the baseline at q=1.82 Å⁻¹ for $\chi = 25^{\circ}$ and $\chi = 40^{\circ}$ are 49 % and 14 % of the scattering intensity at $\chi = 10^{\circ}$. This corresponds to 32 % and 65 % drops in peak heights, respectively, for these oblique angles relative to the 40 oMLD cycle PEDOT condition in Figure 6a. For the 100 oMLD cycle condition in Figure 6c.ii (52.0 nm PEDOT film thickness by SE) the scattering intensity at $\chi = 25^{\circ}$ and $\chi = 40^{\circ}$ are 67% and 30% of the peak scattering intensity at $\chi =$ 10°, respectively. These decreases in intensity are similar to the values we measured for the 40 oMLD cycle PEDOT film in Figure 6a.ii. Together, these data indicate that at 60 oMLD cycles, the smallest fractio nof PEDOT domains are rotated at steeper oblique angles of 25° and 40° relative to surface parallel, with a larger fraction of PEDOT domains oriented at these steeper oblique angles for the 40 and 100 oMLD cycle conditions.

Although previous work has demonstrated that the orientation of oMLD PEDOT domains varies with deposition temperature, this work is the first report that film microstructure (PEDOT domain orientation) varies with thickness for oMLD films formed at a constant deposition temperature. We expect that the formation of more oriented face-on PEDOT films at 60 oMLD cycles (~30 nm) arises because this thickness corresponds to a point at which the thermodynamic driving forces transition from nucleation/surface effects to bulk film growth. In prior studies on oCVD-deposited PEDOT, the orientation of PEDOT domains in thin films has been found to vary with film thickness and temperature. In general, the orientation of PEDOT films transitions from (a) a face-on orientation for thinner (< 50 nm) PEDOT films and higher deposition temperatures to (b) a edge-on orientation for thicker (> 100 nm) PEDOT films and lower deposition temperatures. This prior work indicates that the formation of edge-on films is kinetically controlled, where thicker films are kinetically trapped in an edge-on orientation, and the formation of face-on films is thermodynamically preferred if sufficient thermal energy is provided and the polymer chains are susceptible to reconfiguration to organize in a face-on orientation.

Interestingly, here we identify a new regime where oMLD PEDOT films of < 10 nm thickness also contain a lower fraction of face-on PEDOT domains. We attribute the mixed orientation (Figure 6a) that we observe for <10 nm thick PEDOT films formed using 40 oMLD PEDOT cycles to noncovalent intermolecular effects among PEDOT chains within a confined nanoscale film geometry at < 10 nm thickness. We note that density functional theory studies identify that heteroatom-containing π -aromatic small molecules (similar to EDOT) prefer a T-shaped dimer geometry by ~10-20 kJ/mol over a parallel stacked geometry. Furthermore, thiophene has been found to prefer oblique-angle configurations when clustering in three or four molecule units over two molecule clusters due to additional stabilization from intermolecular interactions. We note that one EDOT monomer is ~0.4 nm in width and ~0.7 nm in length, therefore 9 nm long PEDOT chains correspond to oligomers comprised of ~15 monomer units. We expect that during early nucleation of oMLD PEDOT, these intermolecular interactions between short-chain PEDOT oligomers stabilize off-angle PEDOT chain stacking, whereas as the film thickness increases, the thermodynamics of bulk PEDOT interactions drive face-on orientation.

We note that prior work on oCVD PEDOT films has identified a correlation between PEDOT orientation and electrochemical capacity, where face-on oriented PEDOT exhibits a lower electrochemical capacity.³⁵ This is consistent with the trend we observe here, where the 60 oMLD cycle condition exhibiting the highest degree of face-on orientation exhibits the lowest electrochemical capacity, and the 40 and 100 oMLD cycles both exhibit a lower degree of face-on orientation and higher specific charge capacities. However in this prior work, the lower electrochemical capacity for a face-on PEDOT orientation was attributed to lower electronic conductivity through face-on stacked PEDOT domains. Here, we observe an increase in electrochemical capacity for PEDOT films that exhibit primarily face-on orientation, but contain a significant fraction of PEDOT rotated at oblique angles of up to 40° relative to surface parallel. Differences in conductivity between face-on and edge-on domains do not satisfactorily explain the differences in electrochemical capacity we observe here. Instead, we suggest that this effect originates from differences in ion transfer kinetics, where that the presence of PEDOT at oblique angles of up to 40° allows anions from the electrolyte to insert into the edges of the ordered PEDOT

domains, giving rise to higher electrochemical capacity for the 20 and 40 oMLD cycle films relative to the 60 oMLD cycle film in Figure 5.

To evaluate this hypothesis, we examine the ion insertion kinetics by measuring the charge capacity at varying sweep rates of 10-200 mV/s for PEDOT films deposited using between 20 and 100 oMLD cycles (4-66 nm) in Figure 7. As discussed below, examining the charge capacity at varying sweep rates can be used to determine the extent of diffusion limitations in redox-active materials.⁵² In Figure 7a and 7b, we compare the specific charge capacity vs. sweep rate in NaCl and Na₂SO₄ electrolyte. In general, we find that the trends in electrochemical capacity agree closely between the two electrolytes. We note that, with the exception of the 20 and 40 nm films in Na₂SO₄ electrolyte, 100 CV cycles at 50 mV/s were performed on each of these samples prior to sweep rate analysis to bring the samples to their steady-state electrochemical behavior (see Figure 5). The two thinnest films (20 and 40 oMLD cycles) were measured in Na₂SO₄ electrolyte without 100 CV pre-cycles to evaluate the ion insertion kinetics in the as-formed films. We attribute the lower charge capacities for 20 and 40 oMLD cycles in 0.1 NaCl vs. Na₂SO₄ to degradation in capacity during the 100 CV precycles (see Figure 5). In Figure 7a and 7b, we measure specific charge capacities of ~60 mAh/g at moderate sweep rates (50-200 mV/s) for films formed using 20, 80 and 100 oMLD cycles in NaCl electrolyte and for films formed using 80 and 100 oMLD cycles in Na₂SO₄ electrolyte. These electrochemical capacities are in line with typical charge capacities measured for bulk PEDOT.¹³ We measure maximum specific charge capacities at a sweep rate of 10 mV/s for the 20 oMLD cycle (4 nm) PEDOT film. At this film thickness and sweep rate, we measure specific charge capacities of 116 mAh/g in NaCl after 100 CV cycles, and 151 mAh/g in Na₂SO₄ with no CV pre-cycling in Figure 7a and 7b, respectively. These data further indicate that thinner (< 10 nm) oMLD PEDOT films should be used to maximize specific mass capacity, in line with prior reports of high capacities for thin-film redox-active materials. ^{20,21,52–54}

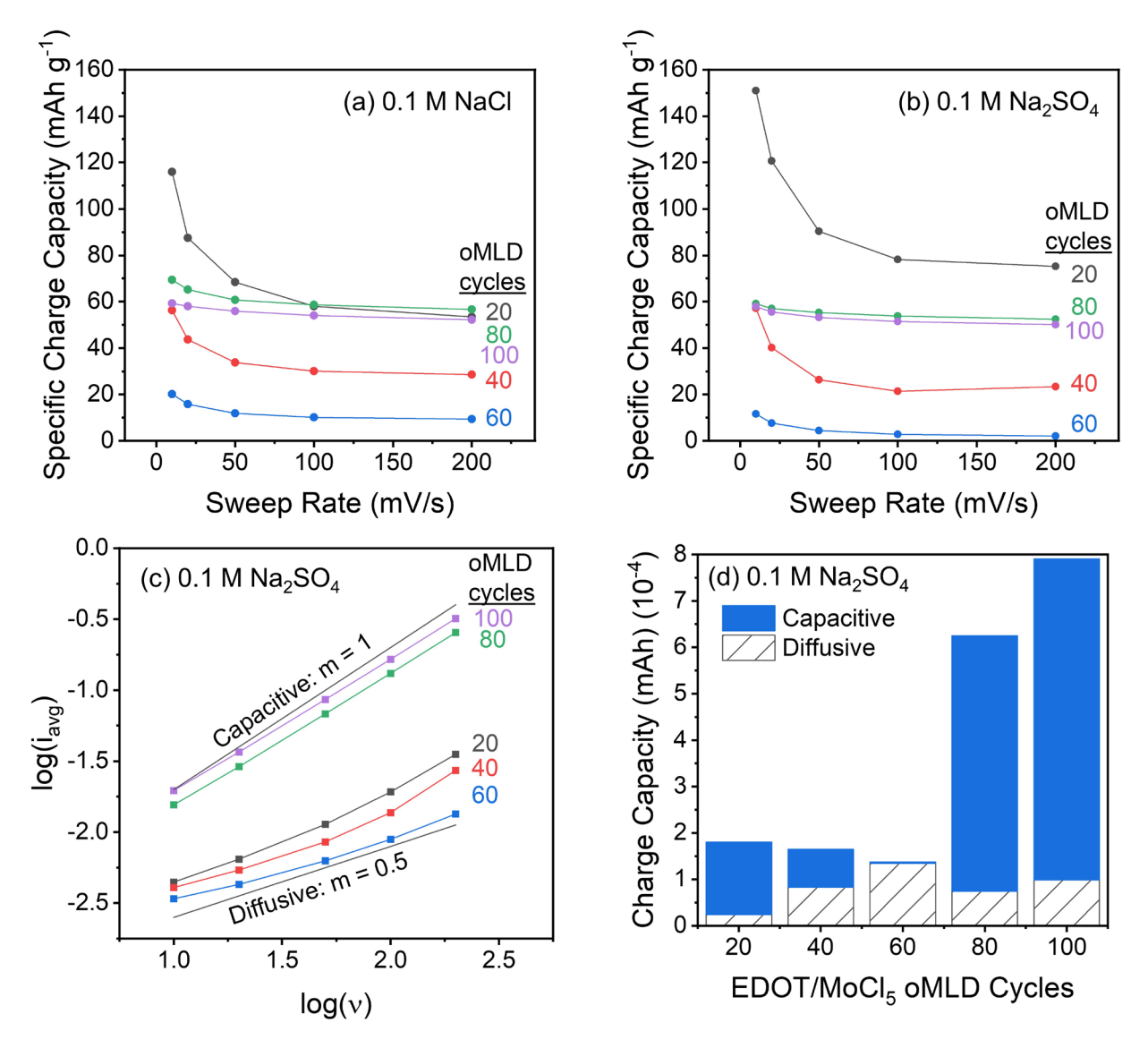


Figure 7. Charge rate analysis of nanoscale thin films of PEDOT grown by oMLD in aqueous (a) 0.1 M NaCl and (b) 0.1 M Na₂SO₄ electrolytes. We analyze the data in (b) using (c) log-log analysis to separate the capacitive and diffusive contributions to charge storage, and (d) plot the relative fractions of capacitive and diffusive contributions to the total charge capacities measured at a sweep rate of 10 mV/s.

Consistent with measurements at a sweep rate of 50 mV/s in Figure 5, we observe the lowest values of specific charge capacities for the 60 oMLD cycle (33 nm) film thickness at all sweep rates in Figure 7a and 7b. At the highest sweep rate of 200 mV/s we observe minimum specific charge capacities for the 60 oMLD cycle (33 nm) film of 9 mAh/g in NaCl and 2 mAh/g in Na₂SO₄. These values are more than 10 and 70 times smaller, respectively, than the maximum values of specific mass capacity observed for the 4 nm oMLD films deposited using 20 oMLD cycles. To evaluate whether these low capacities for the 60 oMLD cycle film arise from an ionic diffusion limitation, we analyze the CV data summarized in Figure 7b employing log-log analysis of average current

 (i_{avg}) vs. sweep rate (v), as shown in Figure 7c. Here, the redox properties of PEDOT are described by a constant phase element (CPE) according to the linear relationship

$$\log(i_{avg}) = (1 - 0.5f_d)\log(v) + \log(A) \tag{1}$$

where f_d is the fraction of diffusive charge storage character and A is a constant related to the specific capacitance of the CPE. ⁵² Thus, in a plot of $\log(i_{avg})$ vs. $\log(v)$, the slope, $m = (1 - 0.5f_d)$, can be used to quantify the fraction of diffusive charge storage behavior, where at m = 0.5 the charge storage is purely diffusive (restricted by ion diffusion), and at m = 1, the charge storage is purely capacitive (no ion diffusion limitation). From this analysis, the "diffusive" fraction of charge storage, f_d , can be interpreted as the amount of charge storage that was rate-limited by ion diffusion. In Figure 7c, we observe that the 80 and 100 oMLD cycle films exhibit nearly ideal capacitive behavior (not diffusion limited), whereas the 60 oMLD cycle film exhibits nearly ideal diffusive behavior (entirely diffusion limited). From Equation 1, we calculate $f_d = 0.62$ for 20 oMLD cycles, $f_d = 0.76$ for 40 oMLD cycles, $f_d = 0.98$ for 60 oMLD cycles, and $f_d = 0.12$ for both 80 and 100 oMLD cycles. We represent this data graphically in Figure 7d, where we plot the charge capacity measured at a sweep rate of 10 mV/s vs. the number of oMLD cycles with the capacity separated into capacitive and diffusive components. The lowest capacity is observed for the 60 oMLD cycle film and is restricted by diffusion limitations ($f_d = 0.98$).

Examining the data in Figure 7d starting at 60 oMLD cycles and progressing down to 20 oMLD cycles, the fraction of diffusion limited capacity decreases and the total charge capacity increases. Likewise, examining the data in Figure 7d starting at 60 oMLD cycles and progressing up to 100 oMLD cycles, the charge capacity starkly increases, with only a small diffusion limitation. The fraction of diffusion limitation across these different film thicknesses is directly proportional to the fraction of face-on oriented domains observed in Figure 6. This analysis reveals that the lower electrochemical capacities observed for face-on oriented PEDOT thin films at ~30 nm film thickness originate from anion diffusion limitations. Here, we suggest that this diffusion limitation arises because anions from the electrolyte must transport through edge planes into the interplane space between PEDOT polymer chains during electrochemical cycling. Face-on PEDOT domains are expected to have fewer edge planes exposed to the electrolyte, which restricts anion transport and reduces electrochemical capacity. We note that the phenomenon we observe here is analogous to orientation-dependent impacts on ion insertion observed previously for layered materials used in lithium ion battery electrodes, such as graphite and lithium cobalt oxide (LiCoO₂).^{66–69} However, this is the first report describing this phenomenon in nanoscale PEDOT films formed by oMLD, and identifying a thickness-dependence for domain orientation that is correlated with this diffusion-limited behavior.

III. Conclusions:

This work establishes the electrochemical charge storage properties of nanoscale (< 100 nm) thin films of PEDOT grown using oMLD. Thickness-dependent microstructural changes are observed over this thickness range and these differences are found to influence the electrochemical properties by affecting ion transport kinetics. These observations have implications for the practical deployment of oMLD PEDOT films in electrochemical devices such as protective

coatings in Li-ion electrode materials, $^{14-16}$ or as active materials in supercapacitors 13,17 or electrochemical water desalination. 18,19 Under the growth conditions explored in this work, fast ion transport and high electrochemical capacities are observed for oMLD PEDOT films of ≤ 10 nm and ≥ 50 nm thickness $^{14-1613,1718,19}$. If intermediate thicknesses of ~ 30 nm are desired, it may be necessary to alter growth conditions or substrate chemistry to achieved edge-exposed PEDOT for rapid ion transfer to/from the electrolyte. The charge storage capacities we observe for ≤ 10 nm and ≥ 50 nm PEDOT thickness are 1.5-2.0 times higher than the typical values reported for PEDOT, and are > 60% of PEDOT's theoretical maximum capacity of 190 mAh/g. We expect that the nanoscale geometry and more favorable molecular structure accessible by oMLD (e.g. without side-chains or additives) allows PEDOT to achieve these high capacities. $^{21,22,351321,2231-33}$ Thickness-dependent changes in microstructure have not been widely considered in previous MLD literature and this study is expected to motivate a range of new studies in this field.

IV. Materials and Methods

Oxidative Molecular Layer Deposition: We employed a hot-walled viscous flow reactor⁷⁰ with precursor configurations for oMLD deposition described previously.^{21,22} The reactor was held at 150°C using PID temperature control and ~0.85 torr of inert argon carrier gas baseline pressure (UHP, 99.999% Ar) is maintained using a mass flow controllers. EDOT (A) and MoCl₅ (B) were each held at 100 °C in stainless steel flow-over bubblers. Unless otherwise noted, one oMLD cycle consisted of an A:Purge:B:Purge dosing sequence employed a timing of 20:100:100:100, with each value in units of seconds. PEDOT was deposited onto PGS and 2 cm by 2 cm silicon flats. To perform each deposition, samples are placed on a stainless steel tray and loaded into the reactor chamber. The samples are heated under continuous argon purge in the reactor for at least 60 minutes prior to deposition.

Spectroscopic Ellipsometry (SE): After oMLD, film thicknesses on silicon flat samples were measured using SE collected at wavelengths of between 300-800 nm at an incident angle 65° using a J.A. Wollam Alpha-SE ellipsometer. SE data analysis and modeling were performed using the CompleteEASE software package. The PEDOT thin films of 0-60 nm thickness (0-100 oMLD cycles) were fit using a Cauchy model of the form $n(\lambda) = A + B/\lambda^2 + C/\lambda^4$ where λ is wavelength and constant values of A= 1.632, B = -2.877 × 10⁻², C = 6. × 10⁻³ were fit by calibrating against NR measurements. Films > 60 nm in thickness (150 and 175 oMLD cycles) were modelled using three Lorentz Oscillators centered at 2.14, 3.06, and 5.07 eV.

Neutron Reflectivity (NR): Neutron reflectivity data was collected using the Grazing Incidence Neutron Spectrometer (GANS)⁷¹ with a wavelength of 2.35 Å at the University of Missouri research Reactor (MURR). Data analysis was performed using the Reflpak software, which utilizes the Parrat Method, accounting for the substrate, film layers, and layer interfaces to compute a fit curve to match the raw reflectivity data. Layer thickness(es) are obtained from Reflpak model fits.

Electrochemical Measurements: After oMLD deposition, PGS samples were cut into \sim 2 cm by \sim 2 cm square pieces, which were placed in a custom glass electrochemical cell with a surface oring seal to expose 1.27 cm² of sample surface area to the electrolyte. A 6 mm graphite rod

(99.9995%, Alfa Aeser) was used as a counter electrode with an Ag/AgCl reference electrode (BASi). Fresh electrolyte solutions of aqueous 0.1 M NaCl or 0.1 M Na₂SO₄ were mixed using 18.2 M Ω deionized water for each electrochemical measurement. These electrolyte solutions were degassed for 30 minutes using Ar and then pipetted into the electrochemical cell under a continuous blanket Ar purge. Electrochemical measurements are performed using a Biologic SP-150 potentiostat.

Raman Spectroscopy: Raman spectroscopy was conducted on PGS samples using a Renishaw inVia Raman Spectrometer with a 633 nm excitation laser. Data was collected over 500-2000 cm^{-1} with a sweeping scan of $10 cm^{-1}/s$ and a laser power of 10.1 mW.

Scanning Electron Microscopy: Following oMLD deposition, film thickness measurements were performed on cleaved PGS samples using a ThermoScientific Helios 5 Hydra operated in immersion mode at 2kV.

Grazing incidence wide angle X-ray measurement: Samples for GIWAXS were prepared on doped Si substrates. Measurements were performed at Brookhaven National Laboratory at the 12-ID Soft Matter Interfaces (SMI) beamline of the National Synchrotron Light Source II (NSLS-II) with a beam energy of 12 keV. The 2D scattering patterns were collected at an X-ray incidence angle of 0.1° with a Pilatus 900 K–W detector with a pixel size of 172 μm placed at 279 mm from the sample.

V. Conflicts of Interest

There are no conflicts to declare.

VI. Acknowledgements

M.J.Y, Q.K.W., and K.B. acknowledge support from the National Science Foundation, Division of Chemical, Bioengineering, Environmental, and Transport Systems through award number 2131282. A.A. appreciates the support of the National Science Foundation Graduate Research Fellowship under Grant No. DGE-1650044. S.K.Y. is grateful for partial support from support the Office of Naval Research (award no. N00014-19-1-2162). This research used resources of the National Synchrotron Light Source II, a U.S. Department of Energy (DOE) Office of Science User Facility operated for the DOE Office of Science by Brookhaven National Laboratory under Contract No. DE-SC0012704. We thank Dr. Gregory Su and Dr. Matthew Landsman from Lawrence Berkeley National Lab, and Dr. Mikhail Zhernenkov (NSLS-II) for assistance at the beamline. We also thank Dr. Patryk Wasik from NSLS-II for assistance with measurement acquisition, analysis and interpretation of GIWAXS data. Any opinions, findings and conclusions or recommendations expressed in this material are those of the authors and do not necessarily reflect the views of the NSF.

VII. References

(1) Groenendaal, L.; Jonas, F.; Freitag, D.; Pielartzik, H.; Reynolds, J. R. Poly(3,4-Ethylenedioxythiophene) and Its Derivatives: Past, Present, and Future. *Advanced*

- *Materials* **2000**, *12*, 481–494. https://doi.org/10.1002/(SICI)1521-4095(200004)12:7<481::AID-ADMA481>3.0.CO;2-C.
- Jonas, F.; Schrader, L. Conductive Modifications of Polymers with Polypyrroles and Polythiophenes. *Synth Met* **1991**, *41*, 831–836. https://doi.org/10.1016/0379-6779(91)91506-6.
- (3) Gerhard, H.; Friedrich, J. Poly(Alkylenedioxythiophene)s New, Very Stable Conducting Polymers. *Advanced Materials* **1992**, *4*, 116–118.
- (4) Dietrich, M.; Heinze, J.; Heywang, G.; Jonas, F. Electrochemical and Spectroscopic Characterization of Polyalkylenedioxythiophenes. *Journal of Electroanalytical Chemistry* **1994**, *369*, 87–92. https://doi.org/10.1016/0022-0728(94)87085-3.
- (5) Damlin, P.; Kvarnström, C.; Ivaska, A. Electrochemical Synthesis and in Situ Spectroelectrochemical Characterization of Poly(3,4-Ethylenedioxythiophene) (PEDOT) in Room Temperature Ionic Liquids. *Journal of Electroanalytical Chemistry* **2004**, *570*, 113–122. https://doi.org/10.1016/j.jelechem.2004.03.023.
- (6) Chen, X.; Inganäs, O. Three-Step Redox in Polythiophenes: Evidence from Electrochemistry at an Ultramicroelectrode. *Journal of Physical Chemistry* **1996**, *100*, 15202–15206. https://doi.org/10.1021/jp9601779.
- (7) Zozoulenko, I.; Singh, A.; Singh, S. K.; Gueskine, V.; Crispin, X.; Berggren, M. Polarons, Bipolarons, and Absorption Spectroscopy of PEDOT. *ACS Appl Polym Mater* **2019**, *1*, 83–94. https://doi.org/10.1021/acsapm.8b00061.
- (8) Ponder, J. F.; Menon, A. K.; Dasari, R. R.; Pittelli, S. L.; Thorley, K. J.; Yee, S. K.; Marder, S. R.; Reynolds, J. R. Conductive, Solution-Processed Dioxythiophene Copolymers for Thermoelectric and Transparent Electrode Applications. *Adv Energy Mater* **2019**, *9*, 1–7. https://doi.org/10.1002/aenm.201900395.
- (9) Chelawat, H.; Vaddiraju, S.; Gleason, K. Conformal, Conducting Poly(3,4-Ethylenedioxythiophene) Thin Films Deposited Using Bromine as the Oxidant in a Completely Dry Oxidative Chemical Vapor Deposition Process. *Chemistry of Materials* **2010**, *22*, 2864–2868. https://doi.org/10.1021/cm100092c.
- (10) Elschner, Andreas. *PEDOT*: Principles and Applications of an Intrinsically Conductive Polymer; CRC Press, 2011.
- (11) Ghafourisaleh, S.; Popov, G.; Leskelä, M.; Putkonen, M.; Ritala, M. Oxidative MLD of Conductive PEDOT Thin Films with EDOT and ReCl5as Precursors. *ACS Omega* **2021**, 6, 17545–17554. https://doi.org/10.1021/acsomega.1c02029.
- (12) Heck, J.; Goding, J.; Portillo Lara, R.; Green, R. The Influence of Physicochemical Properties on the Processibility of Conducting Polymers: A Bioelectronics Perspective. *Acta Biomater* **2022**, *139*, 259–279. https://doi.org/10.1016/j.actbio.2021.05.052.

- (13) Fong, K. D.; Wang, T.; Smoukov, S. K. Multidimensional Performance Optimization of Conducting Polymer-Based Supercapacitor Electrodes. *Sustain Energy Fuels* **2017**, *1*, 1857–1874. https://doi.org/10.1039/c7se00339k.
- (14) Piper, D. M.; Travis, J. J.; Young, M.; Son, S.-B. S. B.; Kim, S. C.; Oh, K. H.; George, S. M.; Ban, C.; Lee, S.-H. S. H. Reversible High-Capacity Si Nanocomposite Anodes for Lithium-Ion Batteries Enabled by Molecular Layer Deposition. *Advanced Materials* **2014**, *26*, 1596–1601. https://doi.org/10.1002/adma.201304714.
- (15) Liu, Q.; Liu, Y.; Zhao, C.; Weng, Q.; Deng, J.; Hwang, I.; Jiang, Y.; Sun, C.; Li, T.; Xu, W.; Du, K.; Daali, A.; Xu, G.; Amine, K.; Chen, G. Conformal PEDOT Coating Enables Ultra-High-Voltage and High-Temperature Operation for Single-Crystal Ni-Rich Cathodes. *ACS Nano* **2022**, *16*, 14527–14538. https://doi.org/10.1021/acsnano.2c04959.
- (16) Zhao, Y.; Sun, X. Molecular Layer Deposition for Energy Conversion and Storage. *ACS Energy Lett* **2018**, *3*, 899–914. https://doi.org/10.1021/acsenergylett.8b00145.
- (17) Kim, J.; Kim, J. H.; Ariga, K. Redox-Active Polymers for Energy Storage Nanoarchitectonics. *Joule* **2017**, *1*, 739–768. https://doi.org/10.1016/j.joule.2017.08.018.
- (18) Pasta, M.; Wessells, C. D.; Cui, Y.; Mantia, F. la; la Mantia, F.; Mantia, F. la. A Desalination Battery. *Nano Lett* **2012**, *12*, 839–843. https://doi.org/10.1021/nl203889e.
- (19) Kim, T.; Gorski, C. A.; Logan, B. E. Low Energy Desalination Using Battery Electrode Deionization. *Environ Sci Technol Lett* 2017, 4, 444–449. https://doi.org/10.1021/acs.estlett.7b00392.
- (20) Wyatt, Q. K.; Young, M. J. Pulsed Electrodeposition of Ultrathin Polyaniline Films and Mechanistic Understanding of Their Anion-Mediated Electrochemical Behavior. *J Electrochem Soc* **2020**, *167*, 110548. https://doi.org/10.1149/1945-7111/aba5d5.
- (21) Wyatt, Q. K.; Vaninger, M.; Paranamana, N. C.; Heitmann, T. W.; Kaiser, H.; Young, M. J. Oxidative Molecular Layer Deposition of Amine-Containing Conjugated Polymer Thin Films. *ACS Appl Polym Mater* **2022**. https://doi.org/10.1021/acsapm.2c00942.
- (22) Wyatt, Q. K.; Brathwaite, K. G.; Ardiansyah, M.; Paranamana, N. C.; Brorsen, K. R.; Young, M. J. Mechanistic Insights into Oxidative Molecular Layer Deposition of Conjugated Polymers. *Chemistry of Materials* 2023, 35, 154–162. https://doi.org/10.1021/acs.chemmater.2c02923.
- (23) Mohammadi, A.; Lundström, I.; Inganäs, O.; Salaneck, W. R. Conducting Polymers Prepared by Template Polymerization: Polypyrrole. *Polymer (Guildf)* **1990**, *31*, 395–399. https://doi.org/10.1016/0032-3861(90)90375-9.
- Bilger, D.; Homayounfar, S. Z.; Andrew, T. L. A Critical Review of Reactive Vapor Deposition for Conjugated Polymer Synthesis. *J Mater Chem C Mater* **2019**, *7*, 7159–7174. https://doi.org/10.1039/c9tc01388a.

- (25) Bhattacharyya, D.; Howden, R. M.; Borrelli, D. C.; Gleason, K. K. Vapor Phase Oxidative Synthesis of Conjugated Polymers and Applications. *J Polym Sci B Polym Phys* **2012**, *50*, 1329–1351. https://doi.org/10.1002/polb.23138.
- (26) Kim, J.; Kim, E.; Won, Y.; Lee, H.; Suh, K. The Preparation and Characteristics of Conductive Poly(3,4-Ethylenedioxythiophene) Thin Film by Vapor-Phase Polymerization. *Synth Met* **2003**, *139*, 485–489. https://doi.org/10.1016/S0379-6779(03)00202-9.
- (27) Lock, J. P.; Im, S. G.; Gleason, K. K. Oxidative Chemical Vapor Deposition of Electrically Conducting Poly(3,4-Ethylenedioxythiophene) Films. *Macromolecules* **2006**, 39, 5326–5329. https://doi.org/10.1021/ma0601130.
- (28) Atanasov, S. E.; Losego, M. D.; Gong, B.; Sachet, E.; Maria, J. P.; Williams, P. S.; Parsons, G. N. Highly Conductive and Conformal Poly(3,4-Ethylenedioxythiophene) (PEDOT) Thin Films via Oxidative Molecular Layer Deposition. *Chemistry of Materials* **2014**, *26*, 3471–3478. https://doi.org/10.1021/cm500825b.
- (29) Volk, A. A.; Kim, J.-S.; Jamir, J.; Dickey, E. C.; Parsons, G. N. Oxidative Molecular Layer Deposition of PEDOT Using Volatile Antimony(V) Chloride Oxidant. *Journal of Vacuum Science & Technology A: Vacuum, Surfaces, and Films* **2021**, 39, 032413. https://doi.org/10.1116/6.0000791.
- (30) Wang, X.; Zhang, X.; Sun, L.; Lee, D.; Lee, S.; Wang, M.; Zhao, J.; Shao-Horn, Y.; Dincă, M.; Palacios, T.; Gleason, K. K. High Electrical Conductivity and Carrier Mobility in OCVD PEDOT Thin Films by Engineered Crystallization and Acid Treatment. *Sci Adv* **2018**, *4*, 1–10. https://doi.org/10.1126/sciadv.aat5780.
- (31) George, S. M.; Yoon, B.; Hall, R. A.; Abdulagatov, A. I.; Gibbs, Z. M.; Lee, Y.; Seghete, D.; Lee, B. H. Molecular Layer Deposition of Hybrid Organic Inorganic Films. **2012**.
- (32) Yoshimura, T.; Tatsuura, S.; Sotoyama, W. Polymer Films Formed with Monolayer Growth Steps by Molecular Layer Deposition. *Appl Phys Lett* **1991**, *59*, 482–484. https://doi.org/10.1063/1.105415.
- (33) George, S. M.; Yoon, B.; Dameron, A. A. Surface Chemistry for Molecular Layer Deposition of Organic and Hybrid Organic–Inorganic Polymers. *Acc Chem Res* **2009**, *42*, 498–508. https://doi.org/10.1021/ar800105q.
- (34) Lock, J. P.; Lutkenhaus, J. L.; Zacharia, N. S.; Im, S. G.; Hammond, P. T.; Gleason, K. K. Electrochemical Investigation of PEDOT Films Deposited via CVD for Electrochromic Applications. *Synth Met* 2007, 157, 894–898. https://doi.org/10.1016/j.synthmet.2007.08.022.
- (35) Moni, P.; Lau, J.; Mohr, A. C.; Lin, T. C.; Tolbert, S. H.; Dunn, B.; Gleason, K. K. Growth Temperature and Electrochemical Performance in Vapor-Deposited Poly(3,4-Ethylenedioxythiophene) Thin Films for High-Rate Electrochemical Energy Storage. *ACS Appl Energy Mater* **2018**, *1*, 7093–7105. https://doi.org/10.1021/acsaem.8b01529.

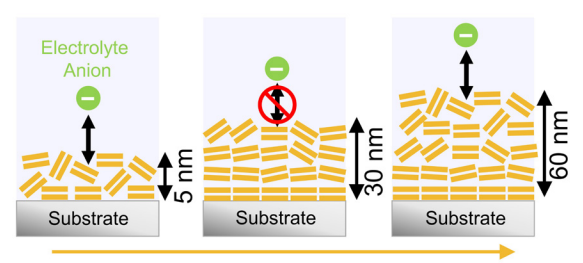
- (36) Zhang, L.; Andrew, T. L. Deposition Dependent Ion Transport in Doped Conjugated Polymer Films: Insights for Creating High-Performance Electrochemical Devices. *Adv Mater Interfaces* **2017**, *4*, 1–9. https://doi.org/10.1002/admi.201700873.
- (37) Wang, X.; Zhang, X.; Sun, L.; Lee, D.; Lee, S.; Wang, M.; Zhao, J.; Shao-Horn, Y.; Dincă, M.; Palacios, T.; Gleason, K. K. High Electrical Conductivity and Carrier Mobility in OCVD PEDOT Thin Films by Engineered Crystallization and Acid Treatment. *Sci Adv* **2018**, *4*. https://doi.org/10.1126/sciadv.aat5780.
- (38) Ghafourisaleh, S.; Popov, G.; Leskelä, M.; Putkonen, M.; Ritala, M. Oxidative MLD of Conductive PEDOT Thin Films with EDOT and ReCl5as Precursors. *ACS Omega* **2021**, 6, 17545–17554. https://doi.org/10.1021/acsomega.1c02029.
- (39) Volk, A. A.; Kim, J.-S.; Jamir, J.; Dickey, E. C.; Parsons, G. N. Oxidative Molecular Layer Deposition of PEDOT Using Volatile Antimony(V) Chloride Oxidant. *Journal of Vacuum Science & Technology A* **2021**, *39*, 032413. https://doi.org/10.1116/6.0000791.
- (40) Im, S. G.; Gleason, K. K. Systematic Control of the Electrical Conductivity of Poly(3,4-Ethylenedioxythiophene) via Oxidative Chemical Vapor Deposition. *Macromolecules* **2007**, *40*, 6552–6556. https://doi.org/10.1021/ma0628477.
- (41) Kienzle, P. A.; Maranville, B. B.; O'Donovan, K. V.; Ankner, J. F.; Berk, N. F.; Majkrzak, C. F. Refl1D https://www.nist.gov/ncnr/reflectometry-software.
- (42) Parratt, L. G. Surface Studies of Solids by Total Reflection of X-Rays. *Physical Review* **1954**, *95*, 359–369. https://doi.org/10.1103/PhysRev.95.359.
- (43) Nicolini, T.; Marquez, A. V.; Goudeau, B.; Kuhn, A.; Salinas, G. In Situ Spectroelectrochemical-Conductance Measurements as an Efficient Tool for the Evaluation of Charge Trapping in Conducting Polymers. *Journal of Physical Chemistry Letters* **2021**, *12*, 10422–10428. https://doi.org/10.1021/acs.jpclett.1c03108.
- (44) Wieland, M.; Malacrida, C.; Yu, Q.; Schlewitz, C.; Scapinello, L.; Penoni, A.; Ludwigs, S. Conductance and Spectroscopic Mapping of EDOT Polymer Films upon Electrochemical Doping. *Flexible and Printed Electronics* **2020**, *5*. https://doi.org/10.1088/2058-8585/ab76e0.
- (45) Singh, V.; Kumar, T. Study of Modified PEDOT:PSS for Tuning the Optical Properties of Its Conductive Thin Films. *Journal of Science: Advanced Materials and Devices* **2019**, *4*, 538–543. https://doi.org/10.1016/j.jsamd.2019.08.009.
- (46) Hwang, J.; Tanner, D. B.; Schwendeman, I.; Reynolds, J. R. Optical Properties of Nondegenerate Ground-State Polymers: Three Dioxythiophene-Based Conjugated Polymers. *Phys Rev B Condens Matter Mater Phys* 2003, 67, 10. https://doi.org/10.1103/PhysRevB.67.115205.
- (47) Hwang, J.; Schwendeman, I.; Ihas, B. C.; Clark, R. J.; Cornick, M.; Nikolou, M.; Argun, A.; Reynolds, J. R.; Tanner, D. B. In Situ Measurements of the Optical Absorption of

- Dioxythiophene-Based Conjugated Polymers. *Phys Rev B Condens Matter Mater Phys* **2011**, *83*, 1–12. https://doi.org/10.1103/PhysRevB.83.195121.
- (48) Niu, L.; Kvarnström, C.; Fröberg, K.; Ivaska, A. Electrochemically Controlled Surface Morphology and Crystallinity in Poly(3,4-Ethylenedioxythiophene) Films. *Synth Met* **2001**, *122*, 425–429. https://doi.org/10.1016/S0379-6779(00)00562-2.
- (49) Aasmundtveit, K. E.; Samuelsen, E. J.; Pettersson, L. A. A.; Inganäs, O.; Johansson, T.; Feidenhans'l, R. Structure of Thin Films of Poly(3,4-Ethylenedioxythiophene). *Synth Met* **1999**, *101*, 561–564. https://doi.org/10.1016/S0379-6779(98)00315-4.
- (50) Hillman, R. A.; Daisley, S. J.; Bruckenstein, S. Solvent Effects on the Electrochemical P-Doping of PEDOT. *Physical Chemistry Chemical Physics* **2007**, *9*, 2379–2388. https://doi.org/10.1039/b618786b.
- (51) Hillman, A. R.; Daisley, S. J.; Bruckenstein, S. Kinetics and Mechanism of the Electrochemical P-Doping of PEDOT. *Electrochem commun* **2007**, *9*, 1316–1322. https://doi.org/10.1016/j.elecom.2007.01.009.
- (52) Young, M. J.; Neuber, M.; Cavanagh, A. C.; Sun, H.; Musgrave, C. B.; George, S. M. Sodium Charge Storage in Thin Films of MnO2 Derived by Electrochemical Oxidation of MnO Atomic Layer Deposition Films, Supplementary Material. *J Electrochem Soc* 2015, 162, A2753–A2761. https://doi.org/10.1149/2.0671514jes.
- (53) Young, M. J.; Schnabel, H.-D.; Holder, A. M.; George, S. M.; Musgrave, C. B. Band Diagram and Rate Analysis of Thin Film Spinel LiMn2O4 Formed by Electrochemical Conversion of ALD-Grown MnO. *Adv Funct Mater* **2016**, *26*, 7895–7907. https://doi.org/10.1002/adfm.201602773.
- (54) Chen, X.; Pomerantseva, E.; Gregorczyk, K.; Ghodssi, R.; Rubloff, G. Cathodic ALD V2O5 Thin Films for High-Rate Electrochemical Energy Storage. *RSC Adv* **2013**, *3*, 4294. https://doi.org/10.1039/c3ra23031g.
- (55) Garreau, S.; Louarn, G.; Buisson, J. P.; Froyer, G.; Lefrant, S. In Situ Spectroelectrochemical Raman Studies of Poly(3,4-Ethylenedioxythiophene) (PEDT). *Macromolecules* **1999**, *32*, 6807–6812. https://doi.org/10.1021/ma9905674.
- (56) Moni, P.; Lau, J.; Mohr, A. C.; Lin, T. C.; Tolbert, S. H.; Dunn, B.; Gleason, K. K. Growth Temperature and Electrochemical Performance in Vapor-Deposited Poly(3,4-Ethylenedioxythiophene) Thin Films for High-Rate Electrochemical Energy Storage. *ACS Appl Energy Mater* **2018**, *1*, 7093–7105. https://doi.org/10.1021/acsaem.8b01529.
- (57) Heydari Gharahcheshmeh, M.; Robinson, M. T.; Gleason, E. F.; Gleason, K. K. Optimizing the Optoelectronic Properties of Face-On Oriented Poly(3,4-Ethylenedioxythiophene) via Water-Assisted Oxidative Chemical Vapor Deposition. *Adv Funct Mater* **2021**, *31*. https://doi.org/10.1002/adfm.202008712.

- (58) Volk, A. A.; Kim, J.-S.; Jamir, J.; Dickey, E. C.; Parsons, G. N. Oxidative Molecular Layer Deposition of PEDOT Using Volatile Antimony(V) Chloride Oxidant. *Journal of Vacuum Science & Technology A* **2021**, *39*, 032413. https://doi.org/10.1116/6.0000791.
- (59) Vidano, R. P.; Fischbach, D. B.; Willis, L. J.; Loehr, T. M. Observation of Raman Band Shifting with Excitation Wavelength for Carbons and Graphites. *Solid State Commun* **1981**, *39*, 341–344. https://doi.org/10.1016/0038-1098(81)90686-4.
- (60) TUINSTRA F; KOENIG JL. Raman Spectrum of Graphite. *Journal of Chemical Physics* **1970**, *53*, 1126–1130. https://doi.org/10.1063/1.1674108.
- (61) Ledinský, M.; Paviet-Salomon, B.; Vetushka, A.; Geissbühler, J.; Tomasi, A.; Despeisse, M.; de Wolf, S.; Ballif, C.; Fejfar, A. Profilometry of Thin Films on Rough Substrates by Raman Spectroscopy. *Sci Rep* **2016**, *6*, 4–10. https://doi.org/10.1038/srep37859.
- (62) Hernández, M. A.; Velasco, J. A.; Asomoza, M.; Solís, S.; Rojas, F.; Lara, V. H. Adsorption of Benzene, Toluene, and p-Xylene on Microporous SiO2. *Ind Eng Chem Res* **2004**, *43*, 1779–1787. https://doi.org/10.1021/ie0204888.
- (63) de Moraes, E. E.; Tonel, M. Z.; Fagan, S. B.; Barbosa, M. C. Density Functional Theory Study of π-Aromatic Interaction of Benzene, Phenol, Catechol, Dopamine Isolated Dimers and Adsorbed on Graphene Surface. *J Mol Model* 2019, 25. https://doi.org/10.1007/s00894-019-4185-2.
- (64) Heydari Gharahcheshmeh, M.; Wan, C. T. C.; Ashraf Gandomi, Y.; Greco, K. v.; Forner-Cuenca, A.; Chiang, Y. M.; Brushett, F. R.; Gleason, K. K. Ultrathin Conformal OCVD PEDOT Coatings on Carbon Electrodes Enable Improved Performance of Redox Flow Batteries. *Adv Mater Interfaces* **2020**, *7*, 1–11. https://doi.org/10.1002/admi.202000855.
- (65) Chen, S.; Petsagkourakis, I.; Spampinato, N.; Kuang, C.; Liu, X.; Brooke, R.; Kang, E. S. H.; Fahlman, M.; Crispin, X.; Pavlopoulou, E.; Jonsson, M. P. Unraveling Vertical Inhomogeneity in Vapour Phase Polymerized PEDOT:Tos Films. *J Mater Chem A Mater* **2020**, *8*, 18726–18734. https://doi.org/10.1039/d0ta06031c.
- (66) Iriyama, Y.; Inaba, M.; Abe, T.; Ogumi, Z. Preparation of C-Axis Oriented Thin Films of LiCoO2 by Pulsed Laser Deposition and Their Electrochemical Properties. *J Power Sources* **2001**, *94*, 175–182. https://doi.org/10.1016/S0378-7753(00)00580-2.
- (67) Yamada, I.; Iriyama, Y.; Abe, T.; Ogumi, Z. Lithium-Ion Transfer on a LixCoO2 Thin Film Electrode Prepared by Pulsed Laser Deposition-Effect of Orientation-. *J Power Sources* **2007**, *172*, 933–937. https://doi.org/10.1016/j.jpowsour.2007.05.072.
- (68) Yamada, Y.; Miyazaki, K.; Abe, T. Role of Edge Orientation in Kinetics of Electrochemical Intercalation of Lithium-Ion at Graphite. *Langmuir* **2010**, *26*, 14990–14994. https://doi.org/10.1021/la1019857.

- (69) Kondo, Y.; Abe, T.; Yamada, Y. Kinetics of Interfacial Ion Transfer in Lithium-Ion Batteries: Mechanism Understanding and Improvement Strategies. *ACS Appl Mater Interfaces* **2022**, *14*, 22706–22718. https://doi.org/10.1021/acsami.1c21683.
- (70) Elam, J. W.; Groner, M. D.; George, S. M. Viscous Flow Reactor with Quartz Crystal Microbalance for Thin Film Growth by Atomic Layer Deposition. *Review of Scientific Instruments* **2002**, *73*, 2981–2987. https://doi.org/10.1063/1.1490410.
- (71) Kaiser, H.; Hamacher, K.; Kulasekere, R.; Lee, W. T.; Ankner, J. F.; DeFacio, B.; Miceli, P. F.; Worcester, D. L. Neutron Inverse Optics in Layered Materials. *Inverse Optics III* **1994**, *2241*, 78–89. https://doi.org/10.1117/12.179750.

For Table of Contents Only:



Increasing pEDOT Thickness